



HAL
open science

Numerical study and experiments on the elasto-visco-plastic bifurcation buckling of thick anisotropic plates

Nicolas Jacquet, Nicolas Tardif, Thomas Elguedj, Christophe Garnier

► **To cite this version:**

Nicolas Jacquet, Nicolas Tardif, Thomas Elguedj, Christophe Garnier. Numerical study and experiments on the elasto-visco-plastic bifurcation buckling of thick anisotropic plates. *Thin-Walled Structures*, 2021, 166, pp.108070. 10.1016/j.tws.2021.108070 . hal-03270386

HAL Id: hal-03270386

<https://hal.science/hal-03270386>

Submitted on 2 Aug 2023

HAL is a multi-disciplinary open access archive for the deposit and dissemination of scientific research documents, whether they are published or not. The documents may come from teaching and research institutions in France or abroad, or from public or private research centers.

L'archive ouverte pluridisciplinaire **HAL**, est destinée au dépôt et à la diffusion de documents scientifiques de niveau recherche, publiés ou non, émanant des établissements d'enseignement et de recherche français ou étrangers, des laboratoires publics ou privés.



Distributed under a Creative Commons Attribution - NonCommercial 4.0 International License

Numerical study and experiments on the elasto-visco-plastic bifurcation buckling of thick anisotropic plates

Nicolas Jacquet^{a,b,*}, Nicolas Tardif^a, Thomas Elguedj^a, Christophe Garnier^b

^aUniv Lyon, INSA-Lyon, CNRS UMR5259, LaMCoS, F-69621, France

^bCEA-DES-IRENE-DTN Cadarache F-13108 Saint-Paul-Lez-Durance, France

Abstract

The present work investigates the elasto-visco-plastic buckling of thick plate structures. Methods to estimate the buckling of thin elasto-visco-plastic shells and plates are proposed in literature. To the knowledge of the authors, only few works present experimental results, and none treat the experimental elasto-visco-plastic buckling of thick plate. Thick rectangular plates are chosen as a structure of interest to study elasto-visco-plastic buckling. A modeling / experimental approach is followed to solve such problem. Buckling experiments at room temperature on thick elasto-visco-plastic plates subjected to compressive load are performed. 3D digital image correlation (3D-DIC) is used to measure displacement fields on plate surface during buckling experiments. The experiments are also modeled through a finite element model. Bodner's approach is coupled to Hencky's deformation theory to predict buckling of elasto-visco-plastic plates. Bifurcation analysis are performed to estimate buckling critical stresses and strains, and buckling modes. Geometrical and loading imperfections are also discussed. A good correlation is observed between numerical results and experiments. The limitation of Bodner's approach is also discussed.

Keywords:

Elasto-visco-plastic, buckling, finite element, bifurcation, experiment, DIC, FEMU

*Corresponding author.

Email address: nicolas.jacquet@insa-lyon.fr (Nicolas Jacquet)

1. Introduction

The integrity of structural components is a major issue for nuclear reactors. In addition to the mechanical loading, the environmental conditions can be extreme in nuclear reactors, especially for sodium fast reactors.

The structural components of such reactors are exposed to high temperature (more than 520°C). The buckling of some structural components has been identified as a failure case under ultimate loading. As many components are made of 316L(N) stainless steel, the rate-dependency of the material must be taken into account in the buckling analysis.

A global strategy was defined in order to answer to this issue. This strategy intends to progress step by step, with experiments on simplified geometries and loading, to finally experiment buckling on elasto-visco-plastic thick shells subjected to external pressure, such as cylinders or spheres. This work presents results obtained on thick rectangular plates subjected to a compressive load. These results are used in order to evaluate the numerical/experimental strategy for a future extension of the buckling prediction method to complex rate-dependent shells.

Structural stability has been studied extensively in the past years. Thin shells and plates were more specifically studied, as they are more likely to buckle in service. Energy based methods were first developed to define bifurcation points on elastic structures. *Hill* defined a theory to assess the stability of plastic solids (see [Hill \(1958\)](#)). This last theory was applied with success to many elastic and plastic solids. Its efficiency is well known on thin structures (see [Yeh and Kyriakides \(1986\)](#) or [Bardi and Kyriakides \(2006\)](#)). Nevertheless, some thick structures, as plates, buckle before reaching *Hill's* bifurcation load. A more accurate estimation of the bifurcation point was achieved using any deformation theory to define the tangent operator of the constitutive law. This last method gives better correlation with experiments than the classical *Hill's* method. This paradox was mentioned and discussed by [Hutchinson and Budiansky \(1976\)](#).

Concerning thick plates buckling, this topic has also been largely studied in the literature. Many articles focus on the buckling of thin rectangular plates like in [Hoff \(1976\)](#), [Bridget](#)

et al. (1934), Bijlaard (1949), Peters (1948) or Romeo and Frulla (1994). In addition to the existing experimental works, many numerical methods were developed to predict the buckling of elasto-plastic plates subjected various loadings and boundary conditions. They all intend to define the critical points of the bifurcation condition obtained through the *Shanley's* concept of continued loading during buckling. This bifurcation condition is defined in Chakrabarty (2000). The different methods approximate the singular solutions of buckling in different ways, through trigonometric functions as in Wang et al. (2001) or using Ritz polynomial function as in Wang and Aung (2007). They are very efficient for simple load cases and simple boundary conditions. More sophisticated approaches were developed in the past years using the variational differential quadrature method as in Hasrati et al. (2019) or Kumar Panda and Ramachandra (2010), or the symplectic superposition method as in Wang et al. (2016). All methods have their own benefits and level of complexity for their implementation, especially for complex material behaviours. In this work the approach described in Wang and Aung (2007) is followed to define a simple and efficient analytical buckling prediction method for thick anisotropic plates.

As long as the material is rate-independent, previous methods can be applied with success to establish the uniqueness of the solution. Rate-dependent materials present a more specific behaviour.

Two approaches exist in literature, one defined by Bodner et al. (1991), the other defined by Triantafyllidis et al. (1997). The first one is relatively simple to implement in any Finite Element (FE) software. This method consists in defining an instantaneous plasticity problem. It gives an estimate of the bifurcation point for rate-dependent solids. The instantaneous plasticity problem is defined through the assumption of a constant strain rate (in time) at buckling initiation.

The method developed by Triantafyllidis et al. (1997) is more rigorous; it gives a sufficient condition of bifurcation for rate-dependent solids. Two examples were treated numerically with this method, *Shanley's* column by Massin et al. (1999) and uniaxial plane strain test by Nestorović et al. (2000). The method suffers of being more complex to implement in a FE software. Because of the high level of fidelity of *Bodner's* approach for thin structures,

Triantafyllidis' method was not investigated in this work. This particular point is discussed in detail later.

Using *Bodner's* hypothesis, the existing methods to analyze the stability of rate-independent materials can be applied to define the stability of the instantaneous plasticity problem. *Bodner's* approach was applied numerically on different geometries by [Paley and Aboudi \(1991\)](#), [Bodner and Naveh \(1988\)](#), [Mikkelsen \(1993\)](#) or [Mikkelsen \(2001\)](#).

Most of the existing works only deal with a theoretical or a numerical approach. Only few works present experimental results on the buckling of rate dependent solids (see [Hoff \(1976\)](#) or [Combescure and Jullien \(2017\)](#)). To the knowledge of the authors, no experimental results were published on the buckling of thick elasto-visco-plastic shells or plates.

This work presents results of buckling experiments performed on thick elasto-visco-plastic rectangular plates subjected to in-plane compressive load. Experiments were performed on various plate geometries and for various displacement rates. A specific instrumentation was used to measure the displacement of the plate surface by 3D Digital Image Correlation (3D-DIC) means. The 3D DIC process is particularly useful to identify the buckling modes and their possible combinations. It is also useful to detect the buckling initiation. Specific discussions are dedicated to these topics and the effect of loading imperfection.

The objective of this paper is also to validate an elasto-visco-plastic buckling criterion based on *Hill's* theory. The criterion couples *Bodner's* hypothesis and *Hencky's* deformation theory for the calculation of the instantaneous tangential behaviour. This method is inspired from the work of [Eslami and Shariyat \(1997\)](#). The criterion was applied through an analytical model to estimate the buckling of thick elasto-visco-plastic rectangular plates subjected to in-plane compressive loading. The numerical buckling estimations were finally compared to the experimental results. The domain of validity of *Bodner's* hypothesis is also discussed in details.

A coupled experimental / numerical approach is proposed to assess the validity of such a criterion. The approach is based on the following ingredients:

- 1. Identification of the elasto-visco-plastic behaviour of the tested material :**

As a matter of fact, the constitutive behaviour of the material strongly affects the buckling predictions. The inverse approach used to identify the elasto-visco-plastic constitutive law of the tested material is presented.

2. **Buckling tests on thick plates made of the elasto-visco-plastic material under uniaxial compressive force** : The initial mid-surface imperfections as well as the evolution of the 3D surface displacement fields were carefully measured. The imperfect boundary conditions and the post buckling mode evolution are extracted from the full field measurement.
3. **Buckling predictions**: The buckling criterion is embedded in an analytical model of a perfect plate under perfect compressive loading. The analytical model is based on the work of [Wang and Aung \(2007\)](#). The identified constitutive law is used in the model.
4. **FE simulation of the buckling tests** : The FE simulations take into account the measured imperfect boundary conditions and the constitutive law of the material. It is first used to validate the identified constitutive law by comparison of the pre-buckling and post buckling plates response. It is also used to derive an out-of-plane displacement based buckling criterion in order to compare the bifurcation results of the buckling tests and the ones of the analytical model.

This article presents the different elements of this experimental / numerical approach. First a brief presentation of the material and its mechanical characterisation is given. Then, the numerical methods and the experimental procedure are introduced. Finally, the results of the buckling experiments and their correlations with the numerical models are presented and discussed.

2. Materials and Experiments

The constitutive law is particularly important to study the buckling of any structure. A model material with an elasto-visco-plastic behaviour at room temperature was selected

instead of the 316L(N). The choice was motivated in order to reduce experimental constraints. As the material behaviour depends on its manufacturing process, we will present it briefly as well as the mechanical characterisation of the model material.

2.1. Specimens manufacturing

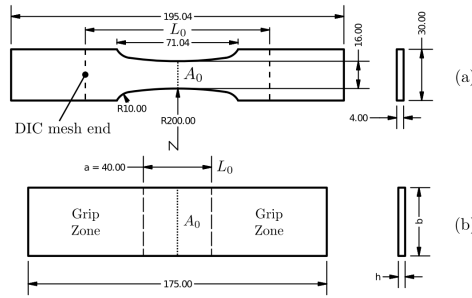


Figure 1: Specimen drawings in mm: (a) Tensile test specimen, (b) Buckling test specimen

The model material is a low melting point alloy commonly named Sn-3.0Ag-0.5Cu or SAC305. It is composed of 96.5% of tin, 3% of silver and 0.5% of copper. Its melting temperature is 217°C. Ingots of $250 \times 90 \times 13 \text{ mm}^3$ were first gravity die cast, water quenched and stress relieved one hour at 100°C, cf. [Wei and Wang \(2012\)](#). This manufacturing process ensures a proper microstructure. Two specimens are extracted from each ingot in order to perform tensile tests or buckling tests. Nine ingots were cast in three sessions for the purpose of this work.

Two types of specimens were machined from the ingots according to the drawings given in [Figure 1](#).

[Figure 1a](#) shows the tensile specimen shape used for the identification of the constitutive law. The shape of the specimen was chosen on purpose, so as to obtain an heterogeneous strain rate field and measure it by DIC during tensile testing. The test data obtained covers a larger strain rate range (equal to a decade of strain rate), which reduces the number of specimens to be tested for creep law identification.

Figure 1b depicts the parametric geometry of specimens used for buckling tests. Buckling specimen offers large grip zones to be installed in a buckling set-up. These large grip zones allow to obtain better boundary conditions. This is essential for plate compressive buckling experiments.

2.2. Material behaviour characterization

2.2.1. Material constitutive law

To model the mechanical behaviour of the SAC 305 alloy, an elasto-visco-plastic constitutive law was chosen. It is characterised by *Hill's* quadratic anisotropic yield criterion, an isotropic hardening modeled by three Voce parameters and a Norton flow rule. While the plastic yield criterion is anisotropic, elasticity is kept isotropic and linear.

The constitutive law is then defined by the set of Equations 1:

$$\begin{aligned}
 \dot{\boldsymbol{\sigma}} &= \mathbf{C} \dot{\boldsymbol{\epsilon}}_e, \\
 \dot{\boldsymbol{\epsilon}} &= \dot{\boldsymbol{\epsilon}}_e + \dot{\boldsymbol{\epsilon}}_p, \\
 \sigma_{eq} &= \sqrt{\boldsymbol{\sigma} : \mathbf{H} : \boldsymbol{\sigma}}, \\
 F &= \sigma_{eq} - R(p), \\
 R(p) &= R_0 + \sum_{i=1}^3 R_i (1 - e^{(-b_i p)}), \\
 \dot{p} &= \left(\frac{F}{\bar{K}} \right)^n,
 \end{aligned} \tag{1}$$

where, $\dot{\boldsymbol{\sigma}}$ is the Cauchy stress rate tensor, $\dot{\boldsymbol{\epsilon}}$ is the strain rate tensor, $\dot{\boldsymbol{\epsilon}}_e$ is the elastic strain rate tensor and $\dot{\boldsymbol{\epsilon}}_p$ is the plastic strain rate tensor, \mathbf{C} is the isotropic elastic linear operator, σ_{eq} is *Hill's* equivalent stress defining the yield surface, \mathbf{H} is *Hill's* tensor (used here for transverse anisotropy), p is the equivalent plastic strain, \dot{p} is the equivalent plastic strain rate and R is the hardening variable.

The material parameters to be identified are $R_0, R_1, b_1, R_2, b_2, R_3, b_3, K, n, \mathbf{H}$ (defined by Lankford's ratio) and \mathbf{C} defined by Young's modulus and Poisson's ratio. Lankford's

ratio is defined by:

$$R_{Lank} = \varepsilon_{yy}/\varepsilon_{zz}, \quad (2)$$

with \mathbf{y} the width direction of the specimen, \mathbf{z} its thickness direction.

2.2.2. FEMU based identification procedure

A Finite Element Model Updating (FEMU) approach was applied to identify the material parameters. This approach compares numerical data from FE simulations to experimental data. The interested reader can find detailed information about this method in [Avril et al. \(2008\)](#).

In our case, tensile tests were performed in order to generate the set of experimental data. These tests were performed on a 20 kN Instron electro-mechanical testing machine at room temperature (20°C). The tests were performed following two weeks after casting in order to limit the material ageing, cf. [Dompierre et al. \(2011\)](#). The displacement rate is maintained constant until the total displacement reaches 4 mm.

Eight specimens from four material batches were produced. Two tensile specimens were manufactured from each material batch. Each specimen was tested according to the testing conditions summarised in [Table 1](#).

2.2.3. Results of constitutive law identification

The identification algorithm was run on each material batch using the test data extracted from the two tensile tests. The material parameters were identified for each material batch. As material discrepancies were observed on test results and on the identified parameters, a reference law was defined. This reference law statistically defines the mechanical behaviour of the SAC 305 associated to its manufacturing process detailed previously. The reference law includes the average behaviour of the identified laws from the four batches as well as their discrepancies.

The characteristics of the material law are presented in [Table 2](#). The minimum and maximum envelopes of the reference law are defined with 95% probability and 90% confidence. This statistical approach is classically used in the MMPDS Handbooks [MMPDS-10 \(2015\)](#).

| Specimen | Speed [mm.s ⁻¹] | Min. strain rate [s ⁻¹] | Max. strain rate [s ⁻¹] | Ingot # | Testing Temperature [°C] |
|----------|-----------------------------|-------------------------------------|-------------------------------------|---------|--------------------------|
| TT/11 | 3.3 10 ⁻³ | 1 10 ⁻⁵ | 1 10 ⁻⁴ | 1 | 20 |
| TT/12 | 3.3 10 ⁻² | 1 10 ⁻⁴ | 1 10 ⁻³ | | 20 |
| TT/21 | 3.3 10 ⁻³ | 1 10 ⁻⁵ | 1 10 ⁻⁴ | 2 | 20 |
| TT/22 | 3.3 10 ⁻² | 1 10 ⁻⁴ | 1 10 ⁻³ | | 20 |
| TT/31 | 3.3 10 ⁻³ | 1 10 ⁻⁵ | 1 10 ⁻⁴ | 3 | 20 |
| TT/32 | 3.3 10 ⁻² | 1 10 ⁻⁴ | 1 10 ⁻³ | | 20 |
| TT/41 | 3.3 10 ⁻³ | 1 10 ⁻⁵ | 1 10 ⁻⁴ | 4 | 20 |
| TT/42 | 3.3 10 ⁻³ | 1 10 ⁻⁴ | 1 10 ⁻³ | | 20 |

Table 1: Summary of tensile testing conditions

K , the Norton coefficient, is linked to \hat{K} , the statistical Norton coefficient, as follows:

$$K \cdot \dot{p}_r^{1/n} = \hat{K} \cdot \dot{p}_r^{1/\bar{n}}, \quad (3)$$

where \bar{n} is the mean experimental Norton exponent, equal to 2.9. \dot{p}_r is the specific experimental strain rate value equal to $2.3 \cdot 10^{-4} \text{s}^{-1}$ used to characterise the creep law discrepancy.

In addition the parameters of the mean reference law are presented in Table 3.

2.2.4. Effect of the cooling rate on the material properties

Each test campaign presented in this work corresponds to a group of batches. A group of batches gathers material batches manufactured at the same time. The three groups of batches (tensile tests, BTC #1 and BTC #2), used to manufacture all the specimens, were manufactured at different times of the year and under different climatic conditions. The temperature of the water used for the quench could have changed by few degrees, as presented in Table 4. A slight modification of the quench temperature can affect the cooling rate as well. [Kim et al. \(2002\)](#) show that the cooling rate has an important impact on the mechanical properties.

| Parameters | Mean | Std.Dev. | Max _{95/90} | Min _{95/90} | Units |
|------------------|-------|----------|----------------------|----------------------|----------------------|
| $\hat{R}(0.005)$ | 16.4 | 0.7 | 18.9 | 13.9 | MPa |
| $\hat{R}(0.010)$ | 18.0 | 0.7 | 20.8 | 15.3 | MPa |
| $\hat{R}(0.020)$ | 19.2 | 0.8 | 22.1 | 16.3 | MPa |
| $\hat{R}(0.050)$ | 20.9 | 0.9 | 24.2 | 17.5 | MPa |
| $\hat{R}(0.100)$ | 21.8 | 1.1 | 25.9 | 17.7 | MPa |
| n | 2.9 | 0.2 | 3.9 | 2.1 | n/a |
| \hat{K} | 133.8 | 5.3 | 154.4 | 115.8 | MPa.s ^{1/n} |
| E | 41513 | n/a | n/a | n/a | MPa |
| R_{Lank} | 1.8 | n/a | n/a | n/a | n/a |
| ν | 0.35 | n/a | n/a | n/a | n/a |

Table 2: Statistical properties of the reference law

One can show that it mainly affects the yield stress R_0 , without affecting the other hardening parameters nor the creep law. For each group of material, the yield stress was identified with a FEMU process. The yield stresses identified for each group of batches are presented in Table 4.

The reference law is used later to compare the buckling experiments with the Finite Element Analysis (FEA) of the experiments or the numerical buckling predictions. The yield stresses identified are used either to normalise the stress values or as yield stress offset in the numerical models.

2.3. Buckling experiments

The experimental set up used for the buckling tests is presented in Figure 2(a). Each end of the specimen are clamped in self-tightening grips. Grips design allows transverse sliding of the specimen. The grips are guided by two columns. The lower grip is positioned on a rigid plate (part of the testing machine) and aligned with the vertical axis of the testing machine. The compressive load is applied through a 20 kN electro-mechanical testing machine which can be operated in displacement or load control. A point load is applied to the upper grip

| Parameters | Mean reference law | Units |
|------------|--------------------|----------------------|
| R_0 | 15.4 | MPa |
| R_1 | 8.6 | MPa |
| b_1 | 396.9 | n/a |
| R_2 | 5.2 | MPa |
| b_2 | 28.9 | n/a |
| R_3 | 8.3 | MPa |
| b_3 | 2166 | n/a |
| K | 137.6 | MPa.s ^{1/n} |
| n | 2.9 | n/a |
| R_{Lank} | 1.79 | n/a |
| E | 41513 | MPa |
| ν | 0.35 | n/a |

Table 3: Material parameters of the mean reference law

using a hemispherical punch. The testing machine displacement and the reaction load are recorded during testing.

The instrumentation of the testing machine is completed by three 12 Mpx cameras with 200 mm lenses. The surface of the specimen was covered by a random speckle pattern characterised by a Gaussian distribution of its grey level. The grey level distribution is defined by its mean value 133 bits and its standard deviation 48 bits. The speckle pattern characteristic size is between 5 px and 17 px.

A 3D-DIC method is applied to measure the displacement fields on the surface of the buckling specimen. A global FE-DIC software called Ufrekles was used (cf. Réthoré (2018)). For all DIC analysis Q4 elements of 40 px mesh size were used.

The cameras are positioned in a manner to have a Region of Interest (ROI) covering the entire surface of the plate, as shown in Figure 2(b). To cover the whole width of the specimen, the cameras are positioned at 20° from their nearest neighbour. The cameras are

| Parameters | Tensile tests | BTC #1 | BTC #2 | Units |
|--------------|---------------|--------|--------|-------|
| R_0 | 15.4 | 14 | 9.9 | MPa |
| Quench temp. | 20 | 22 | 28 | °C |

Table 4: Yield stresses identified for each group of batches, tensile tests campaign, BTC #1: first buckling test campaign and BTC #2: second buckling test campaign

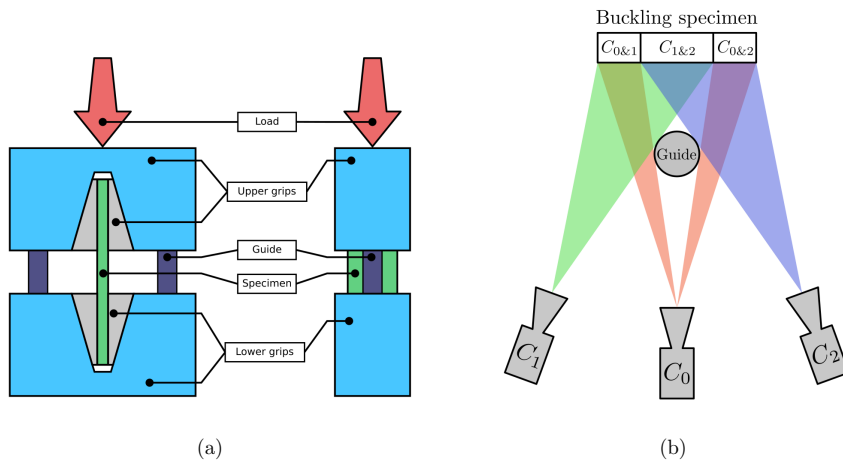


Figure 2: (a) Experimental set up for plate buckling; (b) Positions and coupling of the cameras for DIC (considering test rig environment)

coupled with each other to identify the displacement fields on the surface of the specimen thanks to three 3D-DIC operations.

The plate specimens are characterised by two parameters: the aspect ratio a/b and the thickness ratio b/h . The plate dimensions are presented in Figure 1b. Two aspect ratios are tested, 1.00 and 1.33, while the thickness ratio varies from 15 to 10. All specimens have an effective length a of 40 mm.

During buckling experiment, the testing machine is turned on displacement rate control mode. Three different displacement rates were tested. The testing conditions for the

buckling experiments are summarised in Table 5.

| Specimen | a/b | b/h | Speed [mm.s ⁻¹] | Ingot # | BTC # | Testing Temp. [°C] |
|----------|------|-----|--------------------------------|---------|-------|-----------------------|
| BT1/01 | 1.00 | 10 | 2.10 ⁻³ | 0 | 1 | 20 |
| BT1/02 | 1.33 | 10 | 2.10 ⁻³ | | | 20 |
| BT1/11 | 1.00 | 13 | 2.10 ⁻³ | 1 | | 20 |
| BT1/12 | 1.33 | 10 | 2.10 ⁻³ | 1 | | 20 |
| BT1/21 | 1.00 | 10 | 2.10 ⁻³ | 2 | | 20 |
| BT1/22 | 1.33 | 15 | 2.10 ⁻³ | 2 | | 20 |
| BT2/31 | 1.33 | 10 | 2.10 ⁻² | 3 | 2 | 20 |
| BT2/32 | 1.33 | 10 | 4.10 ⁻⁴ | | | 20 |
| BT2/41 | 1.33 | 10 | 2.10 ⁻² | 4 | | 20 |
| BT2/42 | 1.33 | 10 | 4.10 ⁻⁴ | 4 | | 20 |

Table 5: Summary of plate geometries and testing conditions

Table 5 summarises the geometrical properties of the buckling specimens tested and their testing conditions.

2.4. DIC post-processing

The DIC analysis is performed on the images of the three couples of cameras. The displacement fields identified are then transported to a coordinate system attached to the plate. It is defined as: $(\mathbf{x} - \mathbf{y})$ plane, the best plane going through all DIC nodes identified and \mathbf{x} the axis parallel to the direction of loading. The deviations between the DIC nodes and the ideal plane define the initial geometrical imperfection. Experimental initial geometrical imperfections are ignored in this work, as no significant initial imperfections were observed on the undeformed plate geometry (initial imperfections are lower than 0.005 mm).

Finally, the DIC displacement fields are successively interpolated using polynomial functions and projected on a structured mesh of Q4 elements. This mesh is used later to generate the one of the FEA of the buckling experiments (cf. Figure 4 in Section 3.2). The mesh covers

the entire width of the plate. Axially the mesh does not cover the entire length of the plate; it is limited to the length covered by the DIC mesh.

The displacement fields generated with this method are named experimental displacement fields.

3. Numerical methods

In this section two numerical models are presented. First, an analytical model is used to predict the buckling of thick elasto-visco-plastic plates.

A FE model is also presented. It is used to investigate the effect of loading imperfections and to identify the yield stress decrease in the pre-buckling phase for each experiment.

3.1. Analytical buckling predictions

The stability of rectangular plates subjected to in plane compressive load is analyzed through an analytical model. The model is used to predict the critical values and the associated buckling modes. The plate material behaviour was defined in Section 2.1.

As an elasto-visco-plastic material is used, the strain and stress history need to be defined before any stability analysis. The mechanical equilibrium is solved first, its stability is tested then.

The mechanical equilibrium is solved using the classical *Mises* flow theory, while the buckling prediction uses an instantaneous deformation theory of plasticity.

3.1.1. Numerical modeling of the problem

The Reissner-Mindlin plate theory is used to define the plate kinematics. The set of Equations 4 defines the relation between strain components and displacement fields:

$$\begin{aligned}
 \dot{\epsilon}_{xx} &= \frac{\partial \dot{u}_x}{\partial x} + z \frac{\partial \dot{\phi}_y}{\partial x} \\
 \dot{\epsilon}_{yy} &= \frac{\partial \dot{u}_y}{\partial y} + z \frac{\partial \dot{\phi}_x}{\partial y} \\
 \dot{\gamma}_{xy} &= z \left(\frac{\partial \dot{\phi}_y}{\partial y} + \frac{\partial \dot{\phi}_x}{\partial x} \right) \\
 \dot{\gamma}_{xz} &= \dot{\phi}_y + \frac{\partial \dot{w}}{\partial x} \\
 \dot{\gamma}_{yz} &= \dot{\phi}_x + \frac{\partial \dot{w}}{\partial y}
 \end{aligned} \tag{4}$$

The bending of the plate is characterised by one displacement field w (the out of plane displacement) and two rotation fields ϕ_x and ϕ_y . ϕ_x and ϕ_y are respectively the angles corresponding to the rotation of the shell plane sections around \mathbf{x} and \mathbf{y} .

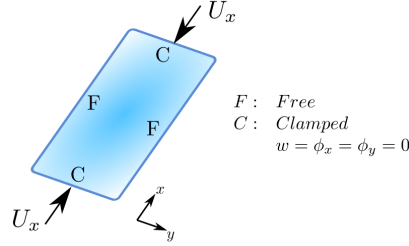


Figure 3: Definition of the plate buckling problem

The plate is constrained as shown in Figure 3. Two opposite edges are free while the two others are clamped (the bending degrees of freedom are constrained). The compressive load is applied through the enforcement of the normal displacement (u_x) on the clamped edges.

Because of the rate dependency of the material, an integration algorithm is used to define the stress state according to the loading history. *Mises* flow theory is used to integrate the constitutive law. A classical radial return mapping integration algorithm was implemented.

This integration algorithm is based on an existing algorithm presented in [Simo and Hughes \(1998\)](#). The integration algorithm was generalised to anisotropic material and additive elasto-visco-plastic behaviour. A plane stress formulation is used, this hypothesis is verified during the pre-buckling phase. Other stress tensor components follow an elastic law.

3.1.2. Buckling prediction

In this paragraph, the method to predict the buckling of thick plates is detailed.

Tangent material law.

A combined approach using *Bodner's* hypothesis with an instantaneous plastic deformation theory is implemented to define the linear tangent operator. This combination was already experimented by [Eslami and Shariyat \(1997\)](#).

Using *Bodner's* hypothesis, the strain rate is considered constant (in time) during buckling (cf. [Bodner et al. \(1991\)](#)). An instantaneous plastic problem is formulated. *Hill's* method is then used to analyze the uniqueness of the instantaneous plastic problem. The instantaneous plastic problem is defined by the following consistency equation:

$$d\dot{p} = d(g(f)) = g'(f)df = 0, \quad (5)$$

where f is the yield criterion and g defines the creep law.

Because of the thickness of the plates, *Hencky's* deformation theory is used to derive the instantaneous tangent operator. This theory correlates better with experimental results for thick plates, see [Hutchinson and Budiansky \(1976\)](#).

Hencky's deformation theory flow rule is defined by:

$$\boldsymbol{\varepsilon}^p = p \frac{\mathbf{H} \boldsymbol{\sigma}}{\sigma_{eq}}. \quad (6)$$

Its variational expression is then written as:

$$\dot{\boldsymbol{\varepsilon}}^p = \frac{\dot{\sigma}_{eq}}{\sigma_{eq}} \left(\frac{\dot{p}}{\dot{\sigma}_{eq}} - \frac{p}{\sigma_{eq}} \right) \mathbf{H} \boldsymbol{\sigma} + p \frac{\mathbf{H} \dot{\boldsymbol{\sigma}}}{\sigma_{eq}}. \quad (7)$$

Using Equation 1, we can write:

$$\begin{aligned}
\dot{\boldsymbol{\sigma}} &= \mathbf{C} \cdot (\dot{\boldsymbol{\varepsilon}} - \dot{\boldsymbol{\varepsilon}}^p), \\
&= \mathbf{C} \cdot \left(\dot{\boldsymbol{\varepsilon}} - \left[\frac{\dot{\sigma}_{eq}}{\sigma_{eq}} \left(\frac{\dot{p}}{\dot{\sigma}_{eq}} - \frac{p}{\sigma_{eq}} \right) \mathbf{H} \boldsymbol{\sigma} + p \frac{\mathbf{H} \dot{\boldsymbol{\sigma}}}{\sigma_{eq}} \right] \right). \tag{8}
\end{aligned}$$

Finally combining Equations 5 and 8, we obtain:

$$\dot{\boldsymbol{\varepsilon}} = \left[\mathbf{C}^{-1} + \frac{p}{\sigma_{eq}} \mathbf{H} + \left(\frac{\dot{p}}{\dot{\sigma}_{eq}} - \frac{p}{\sigma_{eq}} \right) \frac{\mathbf{H} \boldsymbol{\sigma} \otimes \mathbf{H} \boldsymbol{\sigma}}{\sigma_{eq}^2} \right] \dot{\boldsymbol{\sigma}}, \tag{9}$$

and therefore:

$$\mathbf{C}_t = \left[\mathbf{C}^{-1} + \frac{p}{\sigma_{eq}} \mathbf{H} + \left(\frac{\dot{p}}{\dot{\sigma}_{eq}} - \frac{p}{\sigma_{eq}} \right) \frac{\mathbf{H} \boldsymbol{\sigma} \otimes \mathbf{H} \boldsymbol{\sigma}}{\sigma_{eq}^2} \right]^{-1}. \tag{10}$$

\mathbf{C}_t is the tangent operator derived from *Hencky's* deformation theory. This tangent operator is then used to define the critical points and their associated buckling modes.

Uniqueness of the mechanical equilibrium.

To define the uniqueness of the mechanical equilibrium the model developed by [Wang and Aung \(2007\)](#) is used. The uniqueness condition is defined according to [Chakrabarty \(2000\)](#) as follows:

$$\int \Pi \, dV > 0, \tag{11}$$

with:

$$\begin{aligned}
\Pi &= \Pi_i + \Pi_e, \\
\Pi_i &= \boldsymbol{\sigma}^t \cdot \dot{\boldsymbol{\varepsilon}}, \\
\Pi_e &= -\sigma_{xx} \left(\frac{\partial \dot{w}}{\partial x} \right)^2 - \sigma_{yy} \left(\frac{\partial \dot{w}}{\partial y} \right)^2 - 2\sigma_{xy} \left(\frac{\partial \dot{w}}{\partial x} \frac{\partial \dot{w}}{\partial y} \right). \tag{12}
\end{aligned}$$

The singular solutions of Equation 11 are identified using *Ritz's* method, as described by [Wang and Aung \(2007\)](#). The bending displacement and rotation fields are approximated by Ritz polynomial functions:

$$\begin{aligned}
w(x, y) &= \sum_{q=0}^p \sum_{i=0}^q c_m \phi_m^w, \\
\phi_x(x, y) &= \sum_{q=0}^p \sum_{i=0}^q d_m \phi_m^x, \\
\phi_y(x, y) &= \sum_{q=0}^p \sum_{i=0}^q e_m \phi_m^y, \tag{13}
\end{aligned}$$

with:

$$\begin{aligned}
\phi_m^w(x, y) &= \phi_b^w(x/a)^i(y/b)^{q-i}, \\
\phi_m^x(x, y) &= \phi_b^x(x/a)^i(y/b)^{q-i}, \\
\phi_m^y(x, y) &= \phi_b^y(x/a)^i(y/b)^{q-i}.
\end{aligned}
\tag{14}$$

In Equation 13, p is the degree of the polynomial functions. c_m , d_m and e_m are the coefficients of the polynomial functions. ϕ_b^w , ϕ_b^x and ϕ_b^y are functions enforcing the boundary conditions on the plate edges. m is defined by:

$$m = (q + 1) \cdot (q + 2)/2 - i \tag{15}$$

The singular solutions of Equation 11 are obtained by minimising the total potential energy Π with respect to w , ϕ_x and ϕ_y . According to *Ritz*, they respect the following expression:

$$\left[\frac{\partial \Pi}{\partial c_m}, \frac{\partial \Pi}{\partial d_m}, \frac{\partial \Pi}{\partial e_m} \right] = [0, 0, 0]. \tag{16}$$

This last equation can be written as a linear problem:

$$[\mathbf{K}] \cdot \begin{bmatrix} c_m \\ d_m \\ e_m \end{bmatrix} = \mathbf{0}. \tag{17}$$

\mathbf{K} contains the plate geometry, the material behaviour with its tangent operator, the boundary conditions as well as the loading conditions. For a given equilibrium, the modal analysis of \mathbf{K} gives a set of eigenvalues and eigenvectors. The eigenvectors define the singular solutions of Equation 11 while the eigenvalues define the equilibrium uniqueness. An equilibrium is defined as unique if the smallest eigenvalue is positive. If the smallest eigenvalue is negative, the equilibrium is not unique. A critical or bifurcation point is defined by an eigenvalue equal to 0.

Testing the uniqueness of every point on the equilibrium path allows to define every critical point and their associated buckling mode. The first critical point is reached when

the smallest eigenvalue is 0, the second critical point when the second smallest is 0 and so on. We will use this model in section 4 and compare its results with the FE post buckling analysis and the experimental results.

3.2. Finite elements model for post buckling analysis

A FE model was also developed as a link between the analytical model and the buckling experiments. It is used to identify the yield stress decrease in the pre-buckling phase. Its other objective is to evaluate the effect of imperfections on the buckling behaviour of thick plates. Finally, it is also used to compare the analytical buckling predictions with post buckling analysis results.

The FE model was developed with Cast3M, using Mfront to integrate the constitutive law (see Helfer et al. (2015)). SHB8PS elements (Abed-Meraim and Combescure (2002)) are used to model the plate geometry.

The SHB8PS element was implemented in Cast3M and Mfront based on several publications dealing with its formulation, for plasticity, see Abed-Meraim and Combescure (2002, 2009) and for anisotropic plasticity, see Salahouelhadj et al. (2012). The same integration scheme as mentioned in Trinh (2009) is followed to integrate the elasto-visco-plastic constitutive law.

Special case: simulation of each experiment.

The simulation of each experiment is used to identify the yield stress decrease (due to the cooling rate effect during the quench of the ingot) and to investigate the effect of experimental loading imperfections.

To simulate each experiment, it is mandatory to be as close as possible to the experimental conditions. The plate geometry is considered perfectly plane. The initial deviations from the perfectly plane geometry are lower than $5 \mu\text{m}$ with no particular shapes. Initial geometric imperfections are not taken into account for the experiment simulations. The plate dimensions, a , b and h were measured on each specimen and used to build the FE meshes.

The experimental displacement fields are regularised in time and applied to the FE mesh boundaries. The 2D FE mesh is extruded to the plate thickness. The boundary

displacement fields are propagated in the thickness direction according to the Kirchhoff-Love plate kinematic. In order to ignore DIC uncertainties on the FE-DIC mesh boundaries, the rows of elements close to the grips are removed from the FE-DIC mesh to generate the FE mesh, as shown in Figure 4.

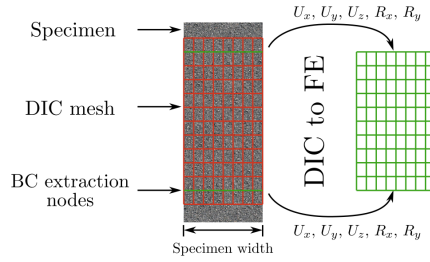


Figure 4: DIC data transfert to FE model

The simulation is stopped when the maximum value of the out of plane displacement field is equal to 75% of the plate thickness. This value is chosen in order to reach buckling, without going too far on this post buckling branch, as it is not the main objective of this work. Only the pre-buckling phase (before collapse of the plate or maximum load) is used to identify the yield stress decrease.

As already mentioned, the reference material law defined in Section 2.2 (cf. Tables 2 and 3) with the associated yield stress decrease (cf. Table 4) is used for all FEA.

4. Results and discussions

In this section, the numerical method to predict buckling of thick plates is evaluated against the experimental results. In a first section the experimental results are analyzed in order to identify the boundary conditions, the loading and the geometrical imperfections. An experimental buckling detection criterion is also defined. It is applied to the experiments to define the experimental critical values. Finally, the experiments are analysed, and the buckling prediction method is evaluated against the experiments with respect to two parameters, the plate geometry and the strain rate.

4.1. Experimental results

All buckling tests were performed in two test campaigns following the testing conditions listed in Table 5. In a first test campaign (BTC #1), we were interested in the effect of plate geometry on its buckling behaviour, while in a second one (BTC #2), the effect of strain rate was investigated. To ease data comparison between all test campaigns, the load data are normalised according to the following expression in the rest of this article.

$$\bar{\sigma} = \frac{F}{A_0} - \bar{R}_0^{BTC \#i}, \quad (18)$$

with F the experimental load, A_0 the initial specimen area and $\bar{R}_0^{BTC \#i}$ the mean yield stress identified for the buckling test campaign #i.

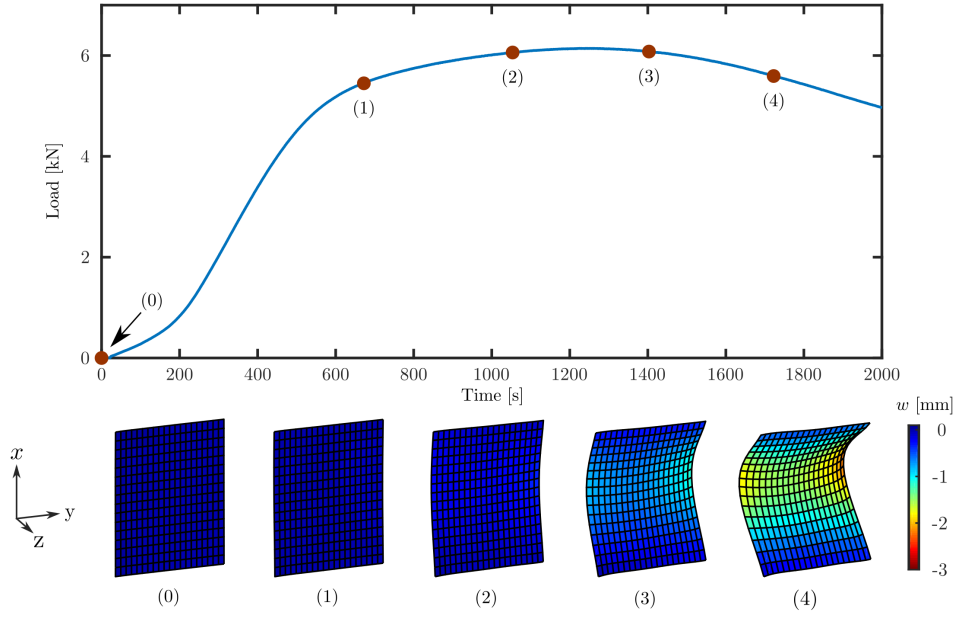


Figure 5: Experimental plate deflection evolution during buckling experiment (BT1/01)

All plate buckling experiments were performed according to the experimental procedure

detailed in Section 2.3. For all plate buckling experiments the load history and the pictures from the three cameras were acquired. The pictures were post processed according to the procedure detailed in Section 2.4.

An example of testing results is presented in Figure 5. The plate deflection is plotted for various times and loads during testing. The coloured plots correspond to the out of plane displacement field.

Despite the explicit 3D illustrations of the plate deformed shapes presented in Figure 5, a 2D cut of the plate deformed configuration is more convenient to describe the buckling modes. Examples of 2D cuts of the plate at the center lines are presented in Figure 6.

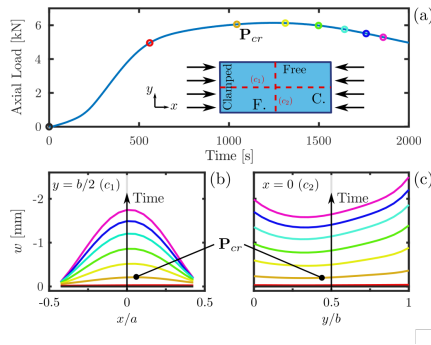


Figure 6: Evolution in time of the experimental out of plane displacement field on both center lines $x = 0$ and $y = b/2$ of the plate (Specimen BT1/01: plate dimensions $a = b = 40$ mm and $h = 4$ mm)

The center lines are defined as the axial ($y = b/2$) and the transverse ($x = 0$) center lines respectively defined by c_1 and c_2 labels in Figure 6. The center lines deflection graphs (Figure 6b and Figure 6c) allow us to identify two geometric properties of the buckling modes. In the x direction, an Euler beam type mode can be observed, while in the y direction a "U shape" type mode is observed.

4.1.1. Boundary conditions and associated imperfections

As classically known, the buckling behaviour of a structure depends on its boundary conditions. Therefore, before any discussion or analysis, the boundary conditions need to be studied. Using the DIC post-processing procedure, the displacement fields close to the grips can be analyzed. Figure 7 presents the positions of the two lines used to characterise the boundary conditions of the plate buckling specimen.

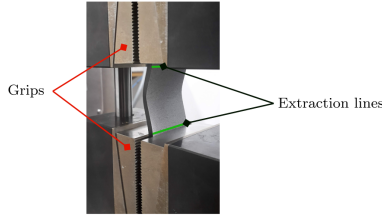


Figure 7: Positions of the extraction lines used to characterize the boundary conditions.

An example of post processed displacement fields on the DIC mesh boundaries is presented in Figures 8(a) and 8(b). The evolutions in time of the displacement and rotation fields presented in Figure 8(a) and Figure 8(b) are defined by:

$$\begin{aligned}
 \Delta U_x &= U_x^{up} - U_x^{low}, \\
 \bar{U}_y &= (U_y^{up} + U_y^{low}) / 2, \\
 \Delta U_z &= U_z^{up} - U_z^{low}, \\
 \hat{\phi}_x &= (\phi_x^{up} + \phi_x^{low}) / 2, \\
 \hat{\phi}_y &= (\phi_y^{up} - \phi_y^{low}) / 2,
 \end{aligned} \tag{19}$$

with the subscript up corresponding to the upper grip and low to the lower one. The rotation fields ϕ_x and ϕ_y are computed using the Kirchhoff-Love plate kinematic. ϕ_x and ϕ_y are respectively the plate rotation fields around \mathbf{x} and \mathbf{y} .

As shown in Figures 8(a) and 8(b), the boundary conditions present some imperfections. The spatial distribution of ΔU_x is not symmetric. The axial displacement (U_x) increases

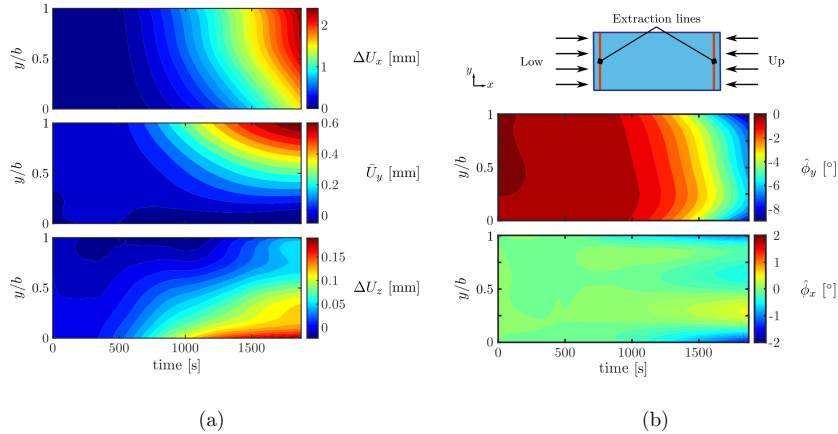


Figure 8: (a) Displacement fields characterizing the loading conditions of plate BT1/01. From top to bottom: ΔU_x , \bar{U}_y and ΔU_z ; (b) Rotation fields characterizing the loading conditions of plate BT1/01. From top to bottom: $\hat{\phi}_y$ and $\hat{\phi}_x$

faster on one side of the plate than on the other side. The same behaviour is observed for ΔU_z . Moreover ΔU_z is not equal to 0. A plate misalignment appears from the beginning of the experiments, despite the guiding system used.

The averaged rotation field, $\hat{\phi}_y$, increases from the beginning of the experiment. Its value is constant with respect to the plate width, except at the end of the experiment (mostly due to the buckling mode). $\hat{\phi}_x$ is almost constant with respect to time, except at the end of the experiment (mostly due to the buckling mode)

The observations made on the boundary conditions of specimen BT1/01 were also observed on the other specimens.

Each source of imperfection has a different impact on the buckling behaviour and its initiation. Two types of imperfection can be identified from the previous observations: the plate misalignment (from ΔU_z) and the plate bending (from $\hat{\phi}_y$). Those two types of imperfection affect the buckling behaviour of the plate differently.

It was identified that the imperfection on $\hat{\phi}_y$ is the main contributor to the buckling.

This is justified as the $\hat{\phi}_y$ imperfection bends the plate in a manner similar to the buckling shape observed. Therefore, it seems that this imperfection helps the plate to buckle. The bending imperfection $\hat{\phi}_y$ is used later to define a buckling initiation criterion.

4.1.2. Experimental buckling initiation criterion

For plates subjected to compressive load, the tangent singularity at the bifurcation point is not always satisfied. This property is often demonstrated in the literature (cf. [Hutchinson and Budiansky \(1976\)](#) and [Wang et al. \(2001\)](#)) by comparing *Mises* flow theory with *Hencky's* deformation theory (DT) in the buckling prediction. The collapsing load is therefore not sufficient to estimate accurately the critical variables.

Post buckling analysis of thick plates.

The tangential bifurcation is illustrated here with a FE post bifurcation analysis. This analysis is focused on the effect of the loading imperfection on the collapse of the plate. A rectangular plate with an aspect ratio of 1.33 and a thickness ratio of 10 is considered here. The plate is subjected to a uni-axial compressive load at constant strain rate. The bending degrees of freedom of the plate (w, ϕ_x, ϕ_y) are constrained at both ends.

A pure bending imperfection is introduced through the rotation ϕ_y at both ends of the plate. The rotation field ϕ_y at each end of the plate is linear with respect to the time. Its value is defined in order to obtain a plate deflection equal to a percentage of the plate thickness at t_f (end of the simulation). It is defined by:

$$\phi_y = \left(R\% \cdot h \frac{4}{a} \right) \frac{t}{t_f}, \quad (20)$$

where $R\%$ is the imperfection amplitude, h the plate thickness, a is the length of the plate, t the time, and t_f the total time.

Several imperfection amplitudes are tested numerically. The bifurcated solutions (coloured curves in [Figure 9a](#)) correspond to a different imperfection amplitude. They are compared to the perfect solution (black curve in [Figure 9a](#)).

First, we see that the collapsing load (i.e. the maximum load) is very dependent on

the imperfection amplitude. It does not converge to a unique value when the imperfection amplitude tends to 0.

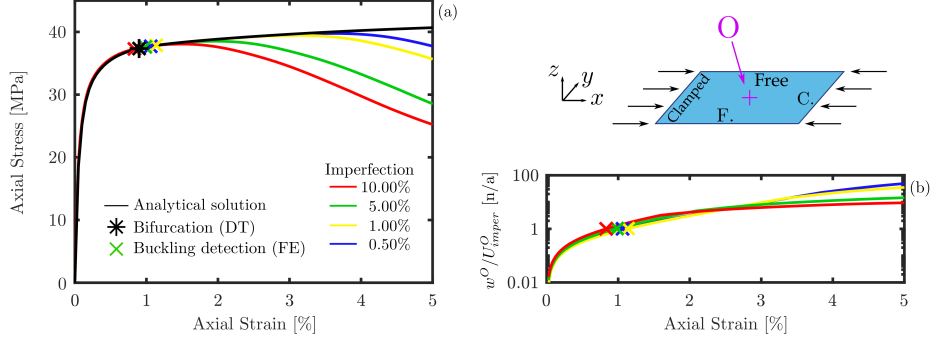


Figure 9: Buckling analysis of a square plate for various loading imperfection amplitudes, comparison of post buckling solutions (FE) and the perfect solution (analytical model); detection of buckling initiation depicted by crosses. (a) axial stress vs. axial strain, (b) imperfection ratio vs. axial strain.

Moreover, the evolution of the plate out of plane displacement at the center (w^O) is analyzed. w^O is normalized by the plate deflection due to the loading imperfection at collapse (U_{imper}^O). U_{imper}^O is defined at plate collapse by:

$$U_{imper}^O = (R\% \cdot h) \frac{t_{collapse}}{t_f}. \quad (21)$$

The normalized plate deflection (w^O/U_{imper}^O) is plotted with respect to the axial strain in Figure 9b for each imperfection amplitude. The equilibrium points corresponding to $w^O = U_{imper}^O$ are identified by crosses in Figure 9.

The identified equilibriums are compared to the bifurcation point computed with the analytical model (black star in Figure 9a). The equilibrium points defined by $w^O = U_{imper}^O$ are close to the bifurcation point for all imperfection amplitudes tested. This condition allows to estimate accurately the equilibrium corresponding to the buckling initiation.

The doubling of the imperfection (i.e. $w^O = U_{imper}^O$) seems to be efficient to detect the buckling initiation of thick elasto-visco-plastic plates. It is also used to assess the experimental critical values.

Application to the experimental detection of buckling.

The criterion corresponding to the doubling of the imperfection ($w^O = U_{imper}^O$) is used to detect the buckling initiation on experiments.

For the experiments, the imperfection at the center of the plate (U_{imper}^O) is linked to the imperfection on $\hat{\phi}_y$ by simple pure bending beam equations as follows:

$$U_{imper}^O = \hat{\phi}_y \frac{a}{4}. \quad (22)$$

The experimental bending imperfection is evaluated at collapse of the plate (i.e. at the maximum load).

The discrepancy of the buckling detection is evaluated through the statistical analysis of ϕ_y in \mathbf{y} direction at both ends of the plate.

This method is used to assess the buckling initiation as well as its discrepancy. As observed numerically, buckling initiates before collapse of the plate, as shown in Figure 6 with the label P_{cr} .

Experimental critical stresses and strains.

Table 6 presents the critical values for each specimen defined with the buckling detection criterion proposed.

As a first observation, the discrepancy on stress data is limited while the discrepancy on the critical displacement and strain is in the same order of magnitude as the DIC process accuracy (0.02 mm). The experimental critical values are discussed in the next subsections.

4.2. Effect of the plate geometry on its buckling behaviour

The effect of the plate geometry on the buckling behaviour is investigated in this subsection. Our discussion will be supported by experimental results from BTC #1 as well as numerical

| Specimen | Mean value | | | Standard deviation | | |
|----------|---------------|-----------------|----------------------|--------------------|-----------------|----------------------|
| | U_{imper}^O | σ_{crit} | ε_{crit} | U_{imper}^O | σ_{crit} | ε_{crit} |
| | [mm] | [MPa] | [%] | [μm] | [MPa] | [%] |
| BT1/01 | 0.24 | 22.3 | 1.67 | 0.04 | 0.2 | 0.17 |
| BT1/02 | 0.12 | 22.1 | 0.83 | 0.02 | 0.1 | 0.04 |
| BT1/11 | 0.08 | 20.5 | 0.95 | 0.02 | 0.1 | 0.07 |
| BT1/12 | 0.10 | 20.5 | 1.05 | 0.01 | 0.1 | 0.03 |
| BT1/21 | 0.21 | 21.6 | 1.58 | 0.05 | 0.2 | 0.15 |
| BT1/22 | 0.07 | 16.4 | 0.53 | 0.01 | 0.1 | 0.02 |
| BT2/31 | 0.15 | 26.6 | 1.12 | 0.03 | 0.1 | 0.04 |
| BT2/32 | 0.08 | 19.7 | 0.69 | 0.02 | 0.2 | 0.06 |
| BT2/41 | 0.17 | 24.6 | 0.80 | 0.01 | 0.1 | 0.03 |
| BT2/42 | 0.10 | 19.5 | 1.10 | 0.01 | 0.1 | 0.02 |

Table 6: Summary of the experimental buckling initiation criterion and critical values

analysis. The plate geometry is defined by its aspect ratio a/b and its thickness ratio b/h . The strain rate is identical for all specimens tested in BTC #1.

4.2.1. FE simulations of the experiments

All experiments were simulated by FEA, with the experimental conditions as an input, as detailed in Section 2.4. The introduction of imperfect experimental conditions in the FE model leads to the collapse of the plate. The load history and the deformed shape extracted from the FE model are compared to the experiments, as presented in Figure 10. In Figure 10, the red plain curve and black dashed curves correspond respectively to the FE and the experimental load histories. The box plots added to the FE load history curve illustrate the effect of the material discrepancy (cf. Table 2) on the numerical load history. The iso-value field plotted in background represents the evolution with respect to time of the out of plane displacement deviation between the FE model and the experiment. The out of plane displacement field is only extracted on the axial center line ($y = b/2$).

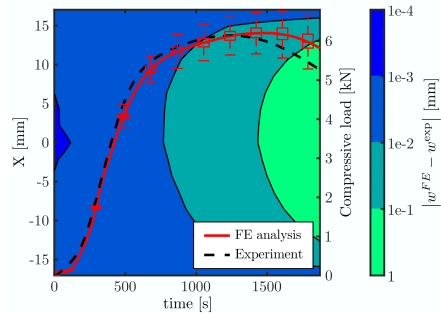


Figure 10: FEA vs. experiment for BT1/01 specimen, Evolution of compressive load and chronograph of the out of plane displacement deviation on the middle line ($y = b/2$) according to time and axial coordinate x

The FEA correlates well with the experiments on both load and out of plane displacement histories, as shown in Figure 10. Both quantities (load and out of plane displacement) start diverging close to the experimental plate collapse. Even if the post buckling evolution can be slightly different, the pre-buckling and the buckling initiation are identical between the FE model and the experiments.

The same behaviour is observed with other specimens from BTC #1. The FE and experimental load histories are presented in Figure 11.

The FE simulations of the experiments tend to validate the relevancy of the identified constitutive law. The reference law well reproduces the structural instability. The experimental buckling behaviour of thick plates and the buckling predictions are discussed in detail in the next subsections.

4.2.2. Comparison of the predicted and experimentally observed critical values

As a reminder the predicted critical values were defined using *Bodner's* hypothesis coupled with a tangent law derived with *Hencky's* deformation theory.

Moreover, 30 randomly generated constitutive laws were used to model the material discrepancy. The random constitutive laws were generated with respect to the statistical description of the reference law (cf. Table 2).

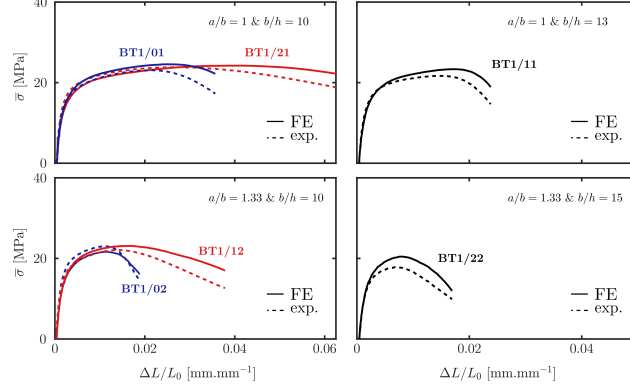


Figure 11: FEA and experimental normalized load according to normalized displacement, for all specimens from BTC #1 (plain curves: FE simulations and dashed curves: experimental data)

The critical stress is normalised in order to better visualise the material discrepancy. This normalisation includes the section dimensions h and b as well as the plate bending rigidity $D = Eh^3/[12(1 - \nu^2)]$.

The experimental normalized critical stresses as well as the critical strains are compared to the buckling predictions in Figure 12. The buckling predictions are defined with the analytical model. The buckling predictions and the critical test data are plotted with respect to the geometrical properties of the plates in Figure 12.

The experimental and predicted normalized critical stresses are presented on the left plots in Figure 12, while right plots present the experimental and predicted critical strains. The plain lines correspond to the analytical predictions of the effective normalized critical stress and strain with respect to the aspect ratio a/b . These predictions are defined with the mean reference law. The dashed curves correspond to the prediction of the minimum and maximum critical stress and strain at 95% probability with 90% confidence. The shaded surfaces correspond to the second and third quartiles of the predicted critical stress and strain. The experimental critical values are depicted by box plots, including discrepancy in

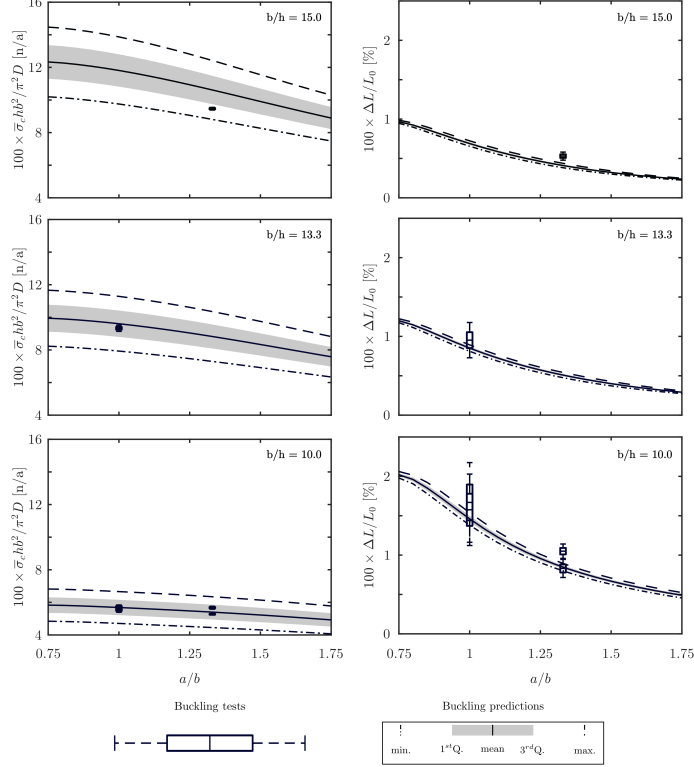


Figure 12: Analytical buckling predictions vs. experimental effective normalized critical stress (left) and critical strain (right), plotted according to the plate aspect ratio and for each plate thickness ratio

the buckling detection (defined in Table 6).

First, while a limited discrepancy is observed on the experimental critical stresses, a large discrepancy is observed on the predicted critical stress. The exact contrary is observed for strain data.

For $b/h = 15$, the thinnest plate, the critical stress is out of the second and third quartile range, but within the min/max envelope. The critical strain data of the same plate ($b/h = 15$) is out of the min/max envelope. This poor correlation can be explained because

of the imperfections and the thickness ratio. Indeed, thin plates are often more sensitive to imperfections. Loading imperfections observed earlier could have initiated the buckling earlier, explaining the poor correlation.

For other thickness ratio, the critical strain predictions are enveloped by the experimental strain data. Errors between predictions and experiments can seem important for some b/h ratio. Nevertheless, these errors are around 0.1% strain, which corresponds to a 0.04 mm displacement in the axial direction of the plate. These errors must be considered with respect to the DIC process used. The DIC uncertainty was evaluated at 0.02 mm. Moreover, the detection criterion is also based on the imperfection amplitude. Depending on when the imperfection is evaluated, it can affect the evaluation of the critical strain. Therefore, the correlation is considered as good on the strain data according to the instrumentation means. The same correlation quality is observed on stress data. The box plots are within the range defined by the second and third quartiles of the buckling predictions.

To conclude on the critical values, except for $b/h = 15$, all experimental critical strains and stresses correlate well with the buckling predictions, as shown in Figure 12.

For the smallest plates ($b/h = 13$ and 15), only one experiment was performed. The generalisation of the results should be considered carefully. Additional experiments would be required in order to generalise these observations.

The effective critical stress and critical strain seem to decrease when the aspect ratio increases. Moreover, the effective critical stress increases with the thickness ratio, and the critical strain decreases with the thickness ratio.

4.2.3. Analysis of the buckling modes

For each specimen, the buckling mode can be extracted from the experimental and FE deformed shape. The buckling modes are extracted from a post buckling deformed shape. They are extracted on both center lines. They are plotted for each plate aspect ratio in Figure 13.

In Figure 13, the plain curves are associated to the FE buckling modes and the dashed curves to the experimental ones. Each colour corresponds to a different plate geometry

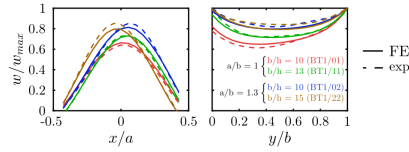


Figure 13: FEA vs. experimental buckling modes, plain curves: FE buckling mode and dashed curves: experimental buckling mode.

(defined by its aspect ratio and its thickness ratio) in Figure 13.

As already observed in Figure 11, the FEA correlate well with experiments. FE and experimental buckling modes coincide as shown in Figure 13. The effect of the plate geometry on the buckling mode can also be observed in Figure 13. On the \mathbf{y} center line ($x = 0$), all modes are very similar and look like Euler beam modes. On the \mathbf{x} center line ($y = b/2$), symmetrical and asymmetrical modes can be observed.

Thick square plates ($a/b = 1$ and $b/h = 10$) present a slight rotation on their buckling modes (red curves in Figure 13) compared to other plate geometries. This particular point is analyzed in the next paragraph.

4.2.4. Mode proximity for thick plates ($b/h = 10$)

Eigen analysis.

For this particular thickness ratio ($b/h = 10$), the critical stress and strain were computed with the analytical model for the three first buckling modes with respect to the plate aspect ratio. The results of this analysis are presented in Figure 14. Red, green and blue curves correspond respectively to the evolution of the critical values for the first, the second and the third modes. The shape of each mode is presented on the right part of Figure 14. The third mode is only plotted from $a/b \geq 0.95$. Before this value the third eigenvalue corresponds to the fourth mode.

The first and the second mode share the same critical values for plates with a low aspect ratio. A mode inversion can also be observed between the third and the second mode in Figure 14 when $a/b = 1.33$. The first mode corresponds to the one generally observed in

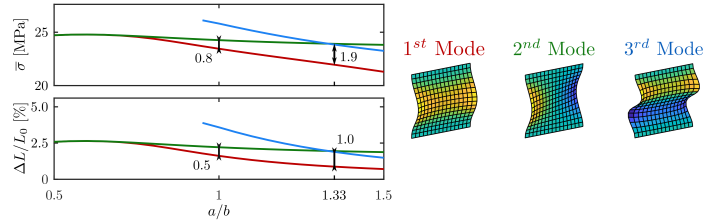


Figure 14: Evolution of critical stress and strain for the first three modes with respect to plate aspect ratio (derived from the analytical model).

the experiments. The second mode is its anti-symmetric shape. The third one is a more energetic mode with two bumps. The difference between the critical stresses of the first two modes is only 0.8 MPa for a square plate and 1.9 MPa for a 1.33 aspect ratio plate. Equally, the difference on the critical strain is 0.5% for a square plate and 1.0% for a 1.33 aspect ratio plate.

The first two modes are very close for a square plate. This proximity could generate a combination of the first two modes at bifurcation, either by simultaneous buckling or successive bifurcations. In both cases, a loading or a geometrical imperfection can ease the apparition of the second mode in the post buckling deformed shape. This point is investigated in the next paragraph.

Post buckling analysis and effect of imperfections.

Using a FE model, two post buckling simulations were performed. Both simulations are identical except on the nature of the initial geometric imperfection.

Case 1: A geometric imperfection derived from the first mode only is applied to a perfect plate. Two plate aspect ratios are investigated, a square plate and a 1.33 aspect ratio plate.

Case 2: A geometric imperfection derived from the first two modes is applied to a perfect plate. Two plate aspect ratios are investigated, a square plate and a 1.33 aspect ratio plate.

In both cases the plates have a thickness ratio equal to 10.

For both cases, the buckling modes are extracted on both center lines and presented in Figure 15. The buckling modes of the 1.33 aspect ratio plate are drawn in Figure 15-2, while

the buckling modes of the square plate are drawn in Figure 15-1.

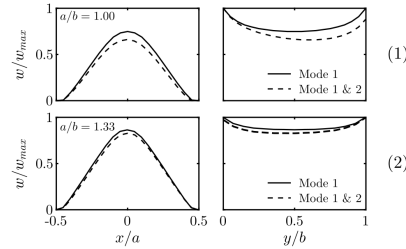


Figure 15: (1) Post buckling modes obtained for a square plate; (2) Post buckling modes obtained for a 1.33 aspect ratio plate (from FEA)

The buckling modes corresponding to **Case 1** are drawn with plain lines. The buckling modes corresponding to **Case 2** are drawn with dashed lines in Figure 15.

As observed experimentally, the buckling mode of the square plate highly depends on the nature of the imperfection. The second mode appears when the nature of the imperfection favours its expression, as shown with the dashed curve in Figure 15-1. The buckling mode shapes of the 1.33 aspect ratio plate are almost not affected by the second buckling mode as shown in Figure 15-2. The first and the second modes are already too far away for the 1.33 aspect ratio plate.

Modes proximity can lead to successive bifurcations as observed experimentally and numerically. This investigation shows the accuracy of the buckling predictions as well as the FE model with respect to the experiments.

4.2.5. Conclusion on the effect of the plate geometry

From this first discussion several observations can be made. The effect of the plate geometry on the buckling behaviour has been observed. The aspect ratio as well as the plate thickness ratio affects the critical values. Moreover, the plate aspect ratio also has an effect on the nature of the buckling mode. This phenomenon was observed experimentally for square plates, successive bifurcations or a simultaneous buckling was observed. The nature of the imperfection can have an important effect on the buckling mode when the first

bifurcation points are close to each other.

The strain rate was held constant for all specimens tested within BTC # 1 and discussed in this section. The next section discusses the effect of the strain rate on the buckling behaviour of thick plates.

4.3. Effect of the strain rate on the buckling of thick plates

The effect of the strain rate on the buckling behaviour is investigated in this section. Only the results of specimens with $a/b = 1.33$ and $b/h = 10$ from BTC #1 and #2 are used. The FE model and the analytical model are used to investigate the effect of strain rate on the buckling behaviour.

Table 7 summarises the testing conditions of the specimens used in this section.

| Specimen ID | a/b | b/h | V [mm.s ⁻¹] | Ingot # | BTC # | V/V _{ref} |
|-------------|------|-----|-------------------------|---------|-------|--------------------|
| BT1/02 | 1.33 | 10 | 2.10 ⁻³ | 0 | 1 | 1 |
| BT1/12 | 1.33 | 10 | 2.10 ⁻³ | 1 | 1 | 1 |
| BT2/31 | 1.33 | 10 | 2.10 ⁻² | 3 | 2 | 10 |
| BT2/32 | 1.33 | 10 | 4.10 ⁻⁴ | 3 | 2 | 1/5 |
| BT2/41 | 1.33 | 10 | 2.10 ⁻² | 4 | 2 | 10 |
| BT2/42 | 1.33 | 10 | 4.10 ⁻⁴ | 4 | 2 | 1/5 |

Table 7: Summary of plate geometries and testing conditions

The variation of the strain rate is characterised by the speed ratio V/V_{ref} , where V is the displacement rate applied and V_{ref} is the displacement rate applied to specimens BT1/02 and BT1/12.

4.3.1. FE simulations of the experiments

As in the previous section the experiments are also simulated with the post buckling FE model. The correlation with the FEA is still very good on load histories as shown in Figures 16 for $V/V_{ref} = 0.2$ and 10. The FE and the experimental curves are close, especially in the pre-buckling phase. The collapse intervenes at similar times (or strains) in the FE

simulations and the experiments. The correlation on the displacement fields is similar to the one presented in Figure 10.

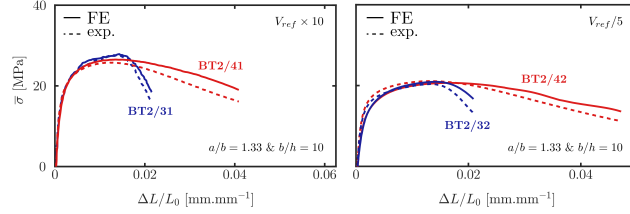


Figure 16: FEA and experimental normalized load according to normalized displacement, for all specimens from BTC #2 (plain curves: FE simulations and dashed curves: experimental data)

4.3.2. Comparison of the predicted and experimentally observed critical values

The experimental critical stresses and strains were also identified for each specimen of BTC #2. The critical values, including buckling detection discrepancy, are presented and compared to the buckling prediction in Figure 17. The buckling predictions were computed with the analytical model. The same normalisation as in the previous section was used for the critical stress.

The box plots in Figure 17 correspond to test data. The mean buckling prediction is plotted with respect to speed ratio (plain curve). As in the previous section the minimum and maximum buckling predictions at 95% with 90% confidence are depicted by dashed curves. Finally, the second and third quartiles are plotted with a shaded surface.

The critical stress increases with the strain rate while the critical strain seems to stay constant in the speed range covered.

The predicted critical stresses correlate well with the experimental ones.

Regarding the critical strains, even if the box plots seem to not comply well with the predictions, the difference is around 0.1% of strain. As previously stated, this difference corresponds to a 0.04 mm displacement in the axial direction. This is of the same order of magnitude as the DIC error of measure.

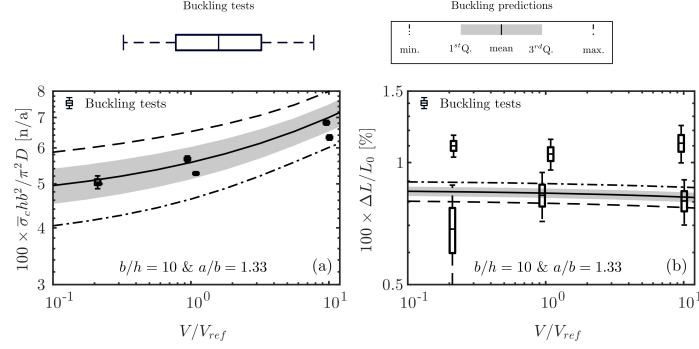


Figure 17: Experimental normalized critical stress and critical strain with respect to speed ratio

To conclude, the predicted critical values correlate well with the experimental ones.

4.3.3. Analysis of the buckling modes

As for specimens from BTC #1 the buckling modes are extracted on both center lines. They are plotted in Figure 18 for each speed ratio.

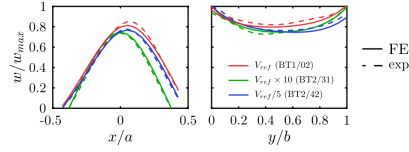


Figure 18: FEA vs. experimental buckling modes, plain curves: FE buckling mode and dashed curves: experimental buckling mode.

First, a good correlation on the buckling modes is also observed between the FEA and the experiments. The buckling modes present identical shapes in Figure 18 for the three displacement rates tested. For the tested plate geometry and in the strain rate range covered, the buckling mode does not seem to be affected by the strain rate.

4.3.4. Validity of Bodner's hypothesis

It is important to notice that the buckling prediction is correct as long as the strain rate stays constant during buckling. This hypothesis is difficult to verify. In this subsection we intend to investigate the validity of *Bodner's* hypothesis.

Critical values from a post buckling analysis for a large strain rate range.

In order to complete the experimental observations, a parametric analysis was performed to investigate the strain rate effect in a larger strain rate range. The buckling predictions from the analytical model were compared to the buckling detection data obtained from a FE post buckling model.

The FE critical values were defined with respect to the buckling detection method presented in subsection 4.1.2. A plate with an aspect ratio of 1.33 and a thickness ratio of 10 was chosen. The speed ratio is the main parameter of this parametric analysis. It varies from 0.01 to 100, which corresponds to a strain rate between $5.0 \times 10^{-7} \text{ s}^{-1}$ and $5.0 \times 10^{-3} \text{ s}^{-1}$. An initial imperfection is applied to the FE model, it is derived from the first buckling mode.

The buckling detection discrepancy is directly linked to the density of probability applied to the geometric imperfection amplitude. This density of probability is modeled by a lognormal distribution. This distribution is characterised by its mean value (5% of the plate thickness) and its standard deviation (5% of the plate thickness).

The results of the parametric analysis are presented in Figure 19. The plain blue curve corresponds to the buckling predictions from the analytical model. The red box plots depict the buckling initiation points detected from the FE post buckling model with respect to the strain rate. In this paragraph, the green box plot of Figure 19 are not discussed, they are commented in the next paragraph.

Even if the critical strain values from the analytical predictions and the FE post buckling model are close, the tendency is inverted. The critical strain detected with the FE model increases when the strain rate increases. The critical strain predicted with the analytical model decreases when the strain rate increases. This inverted tendency can be easily

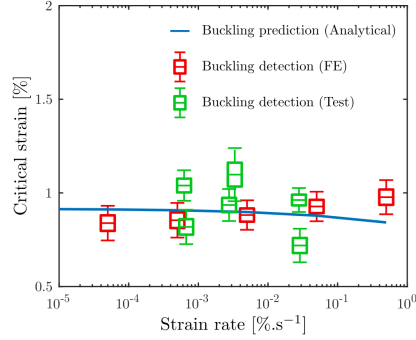


Figure 19: Buckling prediction vs. FE post buckling data, and test data, plate geometry: $a/b = 1.33$ and $b/h = 10$.

explained by the change of strain rate at buckling initiation.

Effect of a rapid strain rate change at buckling.

For elasto-visco-plastic materials when the buckling initiates, the strain rate increases, as for elasto-plastic materials. In elasto-plasticity, this strain rate increase is due to the loss of stiffness caused by the buckling mode shape.

For elasto-visco-plastic materials a rapid strain rate increase implies a rapid increase of the tangent stiffness matrix. This tangent stiffness increase can delay the buckling.

The time scale of the strain rate increase can be compared to the relaxation time of the material. If the strain rate change occurs in a time scale greater than the relaxation time, the effect on the tangential stiffness is negligible. On the contrary, if the strain rate increase occurs in a very small time scale compared to the relaxation time, the stiffness modification cannot be neglected.

A rapid change of strain rate can be introduced in the analytical model through the instantaneous tangent modulus defined by the ratio $\dot{\sigma}_{eq}/\dot{p}$. A Taylor expansion of $\dot{\sigma}_{eq}$ with respect to $\Delta\dot{p}$ can be written as:

$$\begin{aligned}\dot{\sigma}_{eq}(\dot{p} + \Delta\dot{p}) &= \dot{\sigma}_{eq}(\dot{p}) + \frac{\partial \dot{\sigma}_{eq}}{\partial \dot{p}} \Delta\dot{p} \\ &= \dot{\sigma}_{eq}(\dot{p}) + \frac{K}{n} \dot{p}^{1/n-1} \Delta\dot{p}\end{aligned}\quad (23)$$

A new tangent modulus can be defined by:

$$\frac{\dot{\sigma}_{eq}(\dot{p} + \Delta\dot{p})}{\dot{p} + \Delta\dot{p}} = R'(\dot{p}) \frac{\dot{p}}{\dot{p} + \Delta\dot{p}} + \frac{K}{n} \dot{p}^{1/n-1} \frac{\Delta\dot{p}}{\dot{p} + \Delta\dot{p}} \quad (24)$$

This tangent modulus can be considered as the one caused by a rapid change of strain rate at buckling initiation. \dot{p} defines the strain rate from the pre-buckling loading, while $\Delta\dot{p}$ defines the change of strain rate at buckling. Figure 20 shows how the critical strain is affected by the strain rate variation at buckling initiation.

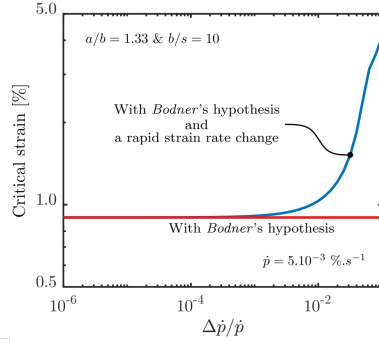


Figure 20: Effect of strain rate variation during buckling on critical strain.

As long as the strain rate change is small, the critical strain is the same as predicted with *Bodner's* hypothesis. In this particular case, for a strain rate change higher than 1%, a significant variation on the critical strain can be observed, as shown in Figure 20.

Bodner's hypothesis seems suitable for small strain rate changes at buckling. For high strain rate changes at buckling, *Bodner's* hypothesis is not accurate anymore. The predictions defined with *Bodner's* hypothesis gives only a lower bound of the bifurcation point.

It seems reasonable to assess that the highest is the strain rate the highest is the strain rate change at buckling. This assumption can explain the inverted tendency observed

in Figure 19. This assumption also limits the usage of *Bodner's* hypothesis to structure subjected to reasonable strain rates.

In addition, the difference between both predictions (analytical and post buckling analysis) is of the same order of magnitude as the experimental discrepancy (between green box plots) in Figure 19. Therefore the predictions defined with *Bodner's* hypothesis seem relevant in a reasonable strain rate range.

4.3.5. Conclusion on the effect of the strain rate

The method implemented here allows to define an estimation of the critical values. To predict more accurately the buckling of thick plates, the deformation theory should be coupled to the methods described by [Triantafyllidis et al. \(1997\)](#). Nevertheless, according to the experiments and the FE modeling, for reasonable strain rates, the present method predicts well the buckling of thick plates. The buckling predictions comply with the experiments and the FEA on both critical values and buckling modes, as shown previously in Figures 11, 12, 13, 16, 17 and 18.

5. Conclusion

This article presented an efficient method to assess the buckling of thick plates with a rate-dependent behaviour. It also experimentally validates the approach inspired from [Eslami and Shariyat \(1997\)](#) as well as the analytical model proposed by [Wang and Aung \(2007\)](#) for the plastic buckling of thick plates.

Two parameters were selected to study the buckling of thick plates: the plate geometry and the strain rate. The experiments were performed according to these two parameters.

An experimental buckling detection criterion was also defined. This criterion is based on the evolution of the singular solution amplitude. This criterion was used to define the experimental critical values.

The DIC instrumentation used for the experiments allowed us to investigate the boundary conditions and to extract the buckling modes for the experimental displacement field.

The prediction model was classically evaluated against the experimental critical values.

In addition, the specific instrumentation used in this work, allowed us to compare the predicted buckling modes to the experimental ones. The validation of the predicted buckling mode as well as the mode proximity observed numerically and experimentally would not have been possible without the DIC instrumentation.

The investigation of the strain rate effect on the buckling behaviour was a major issue. From the results presented in this article, it seems that the strain rate mainly affects the critical values without affecting the buckling mode shape.

The present work also shows the limitation of *Bodner's* hypothesis. For some loading conditions, *Bodner's* hypothesis does not seem relevant. In the case of plates subjected to compressive loading, *Bodner's* hypothesis does not seem relevant for high strain rates. High strain rates could be investigated using the method proposed by [Triantafyllidis et al. \(1997\)](#) in order to validate the tendency observed numerically.

The prediction method presented in this article gives a new experimentally validated tool to predict the buckling of rate dependent thick plates. This method can be used as long as *Bodner's* hypothesis is respected, otherwise it defines a lower bound for the bifurcation point.

Acknowledgements

N. Jacquet was supported by a CEA scholarship. N. Jacquet, N. Tardif and T. Elguedj were partially supported by a research contract with CEA. These supports are gratefully acknowledged.

Appendix A. FEMU identification

The FEMU identification process is based on the flowchart presented in Figure [A.21](#).

This process compares experimental data to numerical ones from a FEA. It takes the experimental data and the material constitutive law as inputs. The parameters of the material constitutive law are defined through an algorithm minimizing the objective function.

The main ingredient of this process is the objective function defined as follows:

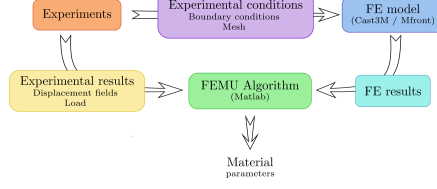


Figure A.21: FEMU method data flow

$$f = \mathbf{R}^t \cdot \mathbf{R}$$

$$\mathbf{R} = \begin{bmatrix} \left(\frac{\mathbf{F}^n - \mathbf{F}^e}{\eta_F} \right) \\ \left(\frac{\boldsymbol{\varepsilon}_{xx}^n - \boldsymbol{\varepsilon}_{xx}^e}{\eta_{\varepsilon_{xx}}} \right) \\ \left(\frac{\boldsymbol{\varepsilon}_{yy}^n - \boldsymbol{\varepsilon}_{yy}^e}{\eta_{\varepsilon_{yy}}} \right) \\ \left(\frac{\boldsymbol{\lambda}^{(i)} - \boldsymbol{\lambda}_0^{(i)}}{C_\lambda^{(i)}} \right) \end{bmatrix} \quad (\text{A.1})$$

with subscript n and e respectively stand for numerical and experimental data. \mathbf{F} contains the value of the reaction load for each increment. $\boldsymbol{\varepsilon}_{xx}$ and $\boldsymbol{\varepsilon}_{yy}$ are vectors containing respectively the strain value at every integration point and for every time increment in \mathbf{x} and \mathbf{y} directions. $\boldsymbol{\lambda}$ and $\boldsymbol{\lambda}_0$ are the vectors containing the material parameters for the current increment and their initial value. Each type of value is normalised by its acceptable error value, η_F , $\eta_{\varepsilon_{xx}}$ and $\eta_{\varepsilon_{yy}}$, as proposed in [Neggers et al. \(2017\)](#). Each component of the material difference vector $(\boldsymbol{\lambda} - \boldsymbol{\lambda}_0)$ is also normalized with respect to an acceptable change of the corresponding parameter during the optimisation process.

References

Abed-Meraim, F., Combescure, A., 2002. SHBSPS—a new adaptative, assumed-strain continuum mechanics shell element for impact analysis. *Computers & Structures* 80, 791–803.

- Abed-Meraim, F., Combescure, A., 2009. An improved assumed strain solid-shell element formulation with physical stabilization for geometric non-linear applications and elastic-plastic stability analysis. *International Journal for Numerical Methods in Engineering* 80, 1640–1686.
- Avril, S., Bonnet, M., Bretelle, A.S., Grédiac, M., Hild, F., Ienny, P., Latourte, F., Lemosse, D., Pagano, S., Pagnacco, E., Pierron, F., 2008. Overview of Identification Methods of Mechanical Parameters Based on Full-field Measurements. *Experimental Mechanics* 48, 381–402.
- Bardi, F.C., Kyriakides, S., 2006. Plastic buckling of circular tubes under axial compression—part I: Experiments. *International Journal of Mechanical Sciences* 48, 830–841.
- Bijlaard, P.P., 1949. Theory and Tests on the Plastic Stability of Plates and Shells. *Journal of the Aeronautical Sciences* 16, 529–541. Publisher: American Institute of Aeronautics and Astronautics .eprint: <https://doi.org/10.2514/8.11851>.
- Bodner, S.R., Naveh, M., 1988. Viscoplastic Shell Buckling, in: Elishakoff, I., Arboez, J., Babcock, C.D., Libai, A. (Eds.), *Studies in Applied Mechanics*. Elsevier. volume 19 of *Buckling of Structures*, pp. 47–60.
- Bodner, S.R., Naveh, M., Merzer, A.M., 1991. Deformation and buckling of axisymmetric viscoplastic shells under thermomechanical loading. *International Journal of Solids and Structures* 27, 1915–1924.
- Bridget, F.J., Jerome, C.C., Vosseller, A.B., 1934. Some New Experiments on Buckling of Thin Wall Construction. *Transactions of the ASME* 56, 569–578. Conference Name: Annual Meeting of the American Society of Mechanical Engineers Meeting Name: Annual Meeting of the American Society of Mechanical Engineers Number: 8 Place: New York, NY Publisher: ASME.
- Chakrabarty, J., 2000. Plastic Buckling, in: *Applied Plasticity*. Springer, New York, NY. *Mechanical Engineering Series*, pp. 459–537.
- Combescure, A., Jullien, J.F., 2017. Creep buckling of cylinders under uniform external pressure: Finite element simulation of buckling tests. *International Journal of Solids and Structures* 124, 14–25.
- Dompierre, B., Aubin, V., Charkaluk, E., Filho, W.C.M., Brizoux, M., 2011. Cyclic mechanical behaviour of Sn3.0Ag0.5Cu alloy under high temperature isothermal ageing. *Materials Science and Engineering: A* 528, 4812–4818.
- Eslami, M.R., Shariyat, M., 1997. Elastic, Plastic, and Creep Buckling of Imperfect Cylinders Under Mechanical and Thermal Loading. *Journal of Pressure Vessel Technology* 119, 27–36. Publisher: American Society of Mechanical Engineers Digital Collection.
- Hasrati, E., Ansari, R., Rouhi, H., 2019. Elastoplastic postbuckling analysis of moderately thick rectangular plates using the variational differential quadrature method. *Aerospace Science and Technology* 91, 479–493.
- Helffer, T., Michel, B., Proix, J.M., Salvo, M., Sercombe, J., Casella, M., 2015. Introducing the open-source mfront code generator: Application to mechanical behaviours and material knowledge management within

- the PLEIADES fuel element modelling platform. *Computers & Mathematics with Applications* 70, 994–1023.
- Hill, R., 1958. A general theory of uniqueness and stability in elastic-plastic solids. *Journal of the Mechanics and Physics of Solids* 6, 236–249.
- Hoff, N.J., 1976. Theory and Experiment in the Creep Buckling of Plates and Shells, in: *Buckling of Structures*. Springer, Berlin, Heidelberg. International Union of Theoretical and Applied Mechanics, pp. 67–77.
- Hutchinson, J.W., Budiansky, B., 1976. Analytical and Numerical Study of the Effects of Initial Imperfections on the Inelastic Buckling of a Cruciform Column, in: *Buckling of Structures*. Springer, Berlin, Heidelberg. International Union of Theoretical and Applied Mechanics, pp. 98–105.
- Kim, K.S., Huh, S.H., Suganuma, K., 2002. Effects of cooling speed on microstructure and tensile properties of Sn–Ag–Cu alloys. *Materials Science and Engineering* 333, 106–114.
- Kumar Panda, S., Ramachandra, L.S., 2010. Buckling of rectangular plates with various boundary conditions loaded by non-uniform inplane loads. *International Journal of Mechanical Sciences* 52, 819–828.
- Massin, P., Triantafyllidis, N., Leroy, Y.M., 1999. On the stability of strain-rate dependent solids.: I—Structural examples. *Journal of the Mechanics and Physics of Solids* 47, 1737–1779.
- Mikkelsen, L.P., 1993. On the analysis of viscoplastic buckling. *International Journal of Solids and Structures* 30, 1461–1472.
- Mikkelsen, L.P., 2001. A Numerical Elastic-Viscoplastic Collapse Analysis of Circular Cylindrical Shells under Axial Compression, in: *IUTAM Symposium on Creep in Structures*. Springer, Dordrecht. *Solid Mechanics and its Applications*, pp. 499–508.
- MMPDS-10, 2015. *Metallic Materials Properties Development and Standardization (MMPDS) Handbook - 10*.
- Neggers, J., Mathieu, F., Hild, F., Roux, S., Swiergiel, N., 2017. Improving full-field identification using progressive model enrichments. *International Journal of Solids and Structures* 118-119, 213–223.
- Nestorović, M.D., Leroy, Y.M., Triantafyllidis, N., 2000. On the stability of rate-dependent solids with application to the uniaxial plane strain test. *Journal of the Mechanics and Physics of Solids* 48, 1467–1491.
- Paley, M., Aboudi, J., 1991. Viscoplastic bifurcation buckling of plates. *AIAA Journal* 29, 627–632.
- Peters, R.W., 1948. Buckling tests of flat rectangular plates under combined shear and longitudinal compression. National Advisory Committee for Aeronautics.
- Réthoré, J., 2018. Ufreckles.
- Romeo, G., Frulla, G., 1994. Nonlinear analysis of anisotropic plates with initial imperfections and various boundary conditions subjected to combined biaxial compression and shear loads. *International Journal*

- of Solids and Structures 31, 763–783.
- Salahouelhadj, A., Abed-Meraim, F., Chalal, H., BALAN, T., 2012. Application of the continuum shell finite element SHB8PS to sheet forming simulation using an extended large strain anisotropic elastic-plastic formulation. *Archive of Applied Mechanics* 82, 1269–1290.
- Simo, J.C., Hughes, T.J.R., 1998. *Computational Inelasticity*. Interdisciplinary Applied Mathematics, Springer-Verlag, New York.
- Triantafyllidis, N., Massin, P., Leroy, Y.M., 1997. A sufficient condition for the linear instability of strain-rate-dependent solids. *Comptes Rendus de l'Académie des Sciences - Series IIB - Mechanics-Physics-Chemistry-Astronomy* 324, 151–157.
- Trinh, V.D., 2009. Development and validation of finite elements of type solid-shells reduced integration stabilized usable for non linear cinematic and behavior problems. Theses. Arts et Métiers ParisTech.
- Wang, B., Li, P., Li, R., 2016. Symplectic superposition method for new analytic buckling solutions of rectangular thin plates. *International Journal of Mechanical Sciences* 119, 432–441.
- Wang, C.M., Aung, T.M., 2007. Plastic buckling analysis of thick plates using p-Ritz method. *International Journal of Solids and Structures* 44, 6239–6255.
- Wang, C.M., Xiang, Y., Chakrabarty, J., 2001. Elastic/plastic buckling of thick plates. *International Journal of Solids and Structures* 38, 8617–8640.
- Wei, G., Wang, L., 2012. Effects of cooling rate on microstructure and microhardness of lead-free Sn-3.0Ag-0.5Cu solder, *IEEE*. pp. 453–456.
- Yeh, M.K., Kyriakides, S., 1986. On the Collapse of Inelastic Thick-Walled Tubes Under External Pressure. *Journal of Energy Resources Technology* 108, 35–47.

Highlights

- Development of a bifurcation buckling criterion for thick elasto-visco-plastic plates subjected to proportional loading.
- Buckling experiments on thick elasto-visco-plastic plates with different shapes and for several strain rates.
- Measurement and post processing of the buckling mode shape through 3D-DIC means, allowing the observation of modes proximity and successive bifurcations.
- Validation of the buckling criterion on both, critical values (stress and strain) and buckling mode shapes.

Nicolas Jacquet : Conceptualization, Methodology, Investigation, Software, Formal analysis, Visualization, Writing – Original Draft **Nicolas Tardif** : Conceptualization, Validation, Resources, Investigation, Supervision, Writing – Review and Editing **Thomas Elguedj** : Validation, Resources, Supervision, Project administration, Writing – Review and Editing **Christophe Garnier**: Validation, Supervision, Project administration, Writing – Review and Editing, Funding acquisition

Conflict of Interest and Authorship Conformation Form

Please check the following as appropriate:

All authors have participated in (a) conception and design, or analysis and interpretation of the data; (b) drafting the article or revising it critically for important intellectual content; and (c) approval of the final version.

This manuscript has not been submitted to, nor is under review at, another journal or other publishing venue.

The authors have no affiliation with any organization with a direct or indirect financial interest in the subject matter discussed in the manuscript

The following authors have affiliations with organizations with direct or indirect financial interest in the subject matter discussed in the manuscript:

Author's name

Affiliation
